minerals

MDPI

Article

Oxidation States of Fe in Constituent Minerals of a Spinel Lherzolite Xenolith from the Tariat Depression, Mongolia: The Significance of Fe^{3+} in Olivine

Terumi Ejima [1,*], Yasuhito Osanai [2], Masahide Akasaka [3], Tatsuro Adachi [2], Nobuhiko Nakano [2], Yoshiaki Kon [4], Hiroaki Ohfuji [5] and Jargalan Sereenen [6]

1 Faculty of Science, Shinshu University, 3-1-1, Asahi, Matsumoto 390-8621, Japan
2 Division of Evolution of Earth Environments, Graduate School of Social, Cultural Studies, Kyushu University, Fukuoka 810-8560, Japan; osanai@scs.kyushu-u.ac.jp (Y.O.); t-adachi@scs.kyushu-u.ac.jp (T.A.); n-nakano@scs.kyushu-u.ac.jp (N.N.)
3 Department of Geoscience, Graduate School of Science and Engineering, Shimane University, Matsue 690-8504, Japan; akasaka@riko.shimane-u.ac.jp
4 Geological Survey of Japan, National Institute of Advanced Industrial Science and Technology (AIST), Tsukuba 305-8567, Japan; yoshiaki-kon@aist.go.jp
5 Geodynamics Research Center, Ehime University, Matsuyama 790-8577, Japan; ohfuji@sci.ehime-u.ac.jp
6 School of Geology and Mining Engineering, Mongolian University of Science and Technology, Ulaanbaatar 14191, Mongolia; jargalan62@yahoo.com
* Correspondence: tejima@shinshu-u.ac.jp; Tel.: +81-0263-37-2505

Received: 26 March 2018; Accepted: 6 May 2018; Published: 9 May 2018

Abstract: The oxidation states of Fe within olivine, orthopyroxene, clinopyroxene, and spinel in a spinel lherzolite xenolith from the Tariat Depression, Mongolia were investigated using ^{57}Fe Mössbauer spectroscopy to evaluate the redox condition of the upper mantle from which the Tariat spinel lherzolite xenolith was derived. The purity of separated minerals for the Mössbauer spectroscopic analysis was examined using X-ray powder diffraction, Raman spectroscopy, and transmission electron microscopy. Average Fo and Fe contents of olivine at the core part of the xenolith are 89.9(4) mol % and 0.195(3) atoms per formula unit, respectively. The $Fe^{3+}/\Sigma Fe$ values of the olivine, orthopyroxene, clinopyroxene, and spinel, determined by Mössbauer spectroscopic analysis, are 0.027(2), 0.15(1), 0.26(3), and 0.34(5), respectively. The Mössbauer spectrum of olivine consists of two doublets assigned to Fe^{2+} at the octahedral sites and one doublet, with *I.S.* of 0.40(2) mm/s and *Q.S.* of 0.69(3) mm/s assigned to Fe^{3+} at the octahedral site. Since the Tariat spinel lherzolite xenolith in this study shows no evidence of metasomatism or thermal alteration, the existence of a small amount of Fe^{3+} in olivine and the fairly high Fe^{3+} contents of clinopyroxene, orthopyroxene, and spinel imply that the upper mantle under the Tariat area was in a rather oxidized condition.

Keywords: spinel lherzolite xenolith; oxidation state of Fe; ^{57}Fe Mössbauer spectroscopy; Mongolia; Tariat Depression

1. Introduction

Oxidation states of Fe within constituent minerals of mantle peridotite can be used as an indicator for the evaluation of redox conditions in the upper mantle, and have been studied repeatedly [1–14]. In some regions of the upper mantle, oxygen fugacity (fO_2) is expected to be higher than that defined by the fayalite + magnetite + quartz buffer (e.g., [2,15]), and a non-negligible amount of ferric iron is contained in orthopyroxene, clinopyroxene, and the spinel of the upper mantle [1–14].

Pyroxene, spinel, and garnet are the most important carriers of Fe^{3+} in the upper mantle [16]: clinopyroxene, orthopyroxene, and spinel in mantle xenoliths have $Fe^{3+}/\Sigma Fe$ values of 0.12–0.33, 0.04–0.09, and 0.05–0.40, respectively [7].

In contrast, olivine, the dominant mineral in the upper mantle, is not allowed to contain trivalent cations such as Fe^{3+} in its structure, in terms of its stoichiometry. In fact, although Banfield et al. [6] detected Fe^{3+} in olivine from metasomatized mantle xenoliths, a source of Fe^{3+} was attributed to submicroscopic intergrowths of laihunite in the olivine. However, Ejima et al. [13] proved the occurrence of Fe^{3+} at the octahedral sites within olivine in a mantle lherzolite xenolith from Oki Island. Ejima et al. [17] suggested that a part of Fe^{2+} within the olivine might have changed to Fe^{3+} by the annealing of the xenoliths by heat from the host magma. Therefore, when we apply the existence of Fe^{3+} in olivine from the mantle xenoliths for the estimation of the redox condition of the upper mantle, an effect of high temperature oxidation during the transportation from the upper mantle to the near surface on the mantle xenoliths has to be taken into consideration.

The Tariat Depression, Mongolia, is a well-known mantle xenolith locality in Central Asia [18]. The spinel in spinel lherzolite xenoliths from Tariat has been known to contain ferric iron ($Fe^{3+}/\Sigma Fe$ = 0.16–0.24 [2]), suggesting a rather high fO_2 condition in the source region of the Tariat spinel lherzolite xenolith. However, the oxidation states of Fe within olivine and other constituent minerals of these xenoliths have not been reported.

In this study, the chemical composition and oxidation states of Fe of olivine, orthopyroxene, clinopyroxene, and spinel in a spinel lherzolite xenolith from Tariat were determined using electron microprobe analysis and ^{57}Fe Mössbauer spectroscopy, respectively, to examine the redox condition of the upper mantle from which the Tariat spinel lherzolite xenolith was derived. In order to evaluate the purity of the separated minerals for the Mössbauer spectroscopic analysis, X-ray powder diffraction, Raman spectroscopic, and transmission electron microscopy (TEM) methods were also used.

2. General Geology and Sampling Site

The Tariat Depression is one of the most typical areas of deep-seated megacrystic xenoliths and mantle-derived xenoliths in the Baikal-Mongolia rift. It is located approximately 500 km southwest of Lake Baikal. The Tariat Depression is mainly characterized by alkalic volcanic rocks of Pliocene, Pleistocene, and Holocene in age. Abundant upper mantle and crustal xenoliths occur in this area [19]. Mantle xenoliths consist of spinel-garnet-bearing websterite, garnet lherzolite, and spinel lherzolite [20]. The sampling site in the present study is located at southeast of Tarkhin Tsagaan Lake (Figure 1).

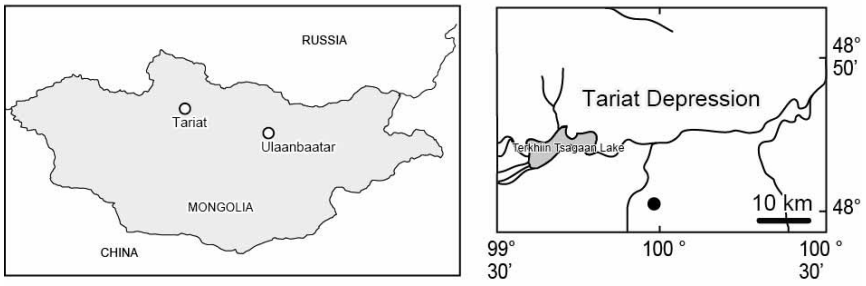

Figure 1. Locations of the Tariat Depression, Mongolia (**left**) and of the sampling site (filled circle) in the Tariat Depression (**right**).

3. Experimental Methods

3.1. Sample Preparation and Purity Evaluation

One thin section from the core of the xenolith and two thin sections from the contact part of the xenolith and the host basalt were prepared for petrographic observations and chemical analysis of constituent minerals.

Olivine, orthopyroxene, clinopyroxene, and spinel grains were separated from the lherzolite xenolith for Mössbauer spectroscopic analyses. Grains of each mineral were dissected out from the core of the xenolith and examined under a binocular microscope to make sure that other minerals are not included. The purities of the separated grains were checked by electron microprobe analysis (EMPA), X-ray powder diffraction (XRD) analysis, and Raman spectroscopy. The separated grains were manually crushed into powder using an agate pestle and mortar.

3.2. Electron Microprobe Analysis

Chemical compositions of minerals were determined using JEOL JXA-8530M electron microprobe analyzer (JEOL, Tokyo, Japan) at Kyushu University and National Institute of Advanced Industrial Science and Technology of Japan (AIST), operated at an accelerating voltage of 15 kV, with a beam current of 20 nA and a beam diameter of 5 μm. The standard materials were diopside for Si (K_α), Mg (K_α), and Ca (K_α); and rutile for Ti (K_α), sanidine for Al (K_α), Cr_2O_3 for Cr (K_α), almandine for Fe (K_α), bustamite for Mn (K_α), NiO for Ni (K_α), and anorthite for Na (K_α).

3.3. Raman Spectroscopy

Raman spectra were measured using the Ram532 micro-Raman spectroscopy system (JASCO, Tokyo, Japan) at Kyushu University. Excitation was by means of the 532 nm line of a solid-state ion laser with an output power of 20 mW. The instrument was equipped with a microscope with a focal spot size of 2 μm.

3.4. Transmission Electron Microscopy (TEM)

To evaluate purity of the olivine, nanoscale observation of an olivine grain in the thin section was performed using high-resolution TEM (HR-TEM). A TEM foil, about 5 μm × 11 μm × 0.1 μm in size, was prepared from an olivine sample using a JOEL JEM-9310 (JEOL, Tokyo, Japan) focused ion beam (FIB) system at Ehime University. The detailed FIB milling procedure for TEM foil preparation is described elsewhere [21]. TEM and HR-TEM observations were carried out with a JEOL JEM-2010 (JEOL, Tokyo, Japan) at Ehime University, operated at 200 kV. Selected-area electron diffraction (SAED) and bright-field imaging were employed to characterize the microstructure of the sample.

3.5. X-ray Powder Diffraction Measurement and Rietveld Analysis

XRD data of olivine, orthopyroxene, and clinopyroxene were collected at Shimane University using a Rigaku RINT automated Bragg-Brentano diffractometer system equipped with a curved graphite diffracted-beam monochromator (RIGAKU, Tokyo, Japan). The Cu X-ray tube generator for CuK_α radiation was operated at 35 kV and 25 mA. The profile was taken in a 2θ range between 10° and 120°, using the step-scan method with a step interval of 0.02° and a count time of 5 s per step. XRD data of spinel was collected at AIST using a Rigaku RINT-automated Bragg-Brentano diffractometer system at AIST, equipped with a curved graphite diffracted-beam monochromator. The rotating anticathode Cu X-ray tube generator for CuK_α radiation was operated at 40 kV and 30 mA. The profile was measured in a 2θ range between 10° and 120° with a step interval of 0.02° and a count time of 5 s per step.

The measured XRD data of olivine were analyzed by the Rietveld method using the RIETAN-FP program by Izumi and Momma [22]. The modified split pseudo-Voigt function was used as the profile function, and correction for preferred orientation was done by using the March-Dollase function [23].

3.6. ^{57}Fe Mössbauer Spectroscopy

Powdered samples of the separated olivine, clinopyroxene, orthopyroxene, and spinel grains from the core of the xenolith were analyzed by ^{57}Fe Mössbauer spectroscopy (TOPOLOGIC SYSTEMS, Tokyo, Japan) to determine the oxidation state and distribution of Fe in each crystallographic site. The Mössbauer spectra were measured at room temperature in the Doppler velocity range of −4 to

4 mm/s at Shimane University, using 370 MBq ^{57}Co in Pd as a source. The absorber was about 20 mg of finely ground sample. The Mössbauer data were obtained with a constant acceleration spectrometer fitted with a 1024 multichannel analyzer. The isomer shift is relative to metallic iron foil. The QBMOSS program of Akasaka and Shinno [24] was used for computer analysis. The quality of the fit was judged from the χ^2 value and standard deviations of the Mössbauer parameters.

4. Results

4.1. Petrography

The studied spinel lherzolite xenolith sample is about 10 cm in diameter. It has a porphyroclastic texture and consists of olivine, orthopyroxene, clinopyroxene, and spinel (Figure 2). The olivine is euhedral to subhedral in form and about 1–4 mm in size (Figure 2a–d). Kink-bands are present in the olivine crystals. The orthopyroxene is subhedral in form and about 0.2–6 mm in size (Figure 2a). The spinel is anhedral in form and about 0.5–3 mm in size (Figure 2c). Clinopyroxene is subhedral to anhedral in form and about 0.2–5 mm in size, and has the rim consisting of diopside and glass (Figure 2a,c). Near the surface of the spinel lherzolite xenolith that is in contact with the host basalt, orthopyroxene has a reaction rim, and the clinopyroxene has been completely broken into diopside and glass (Figure 2e,f).

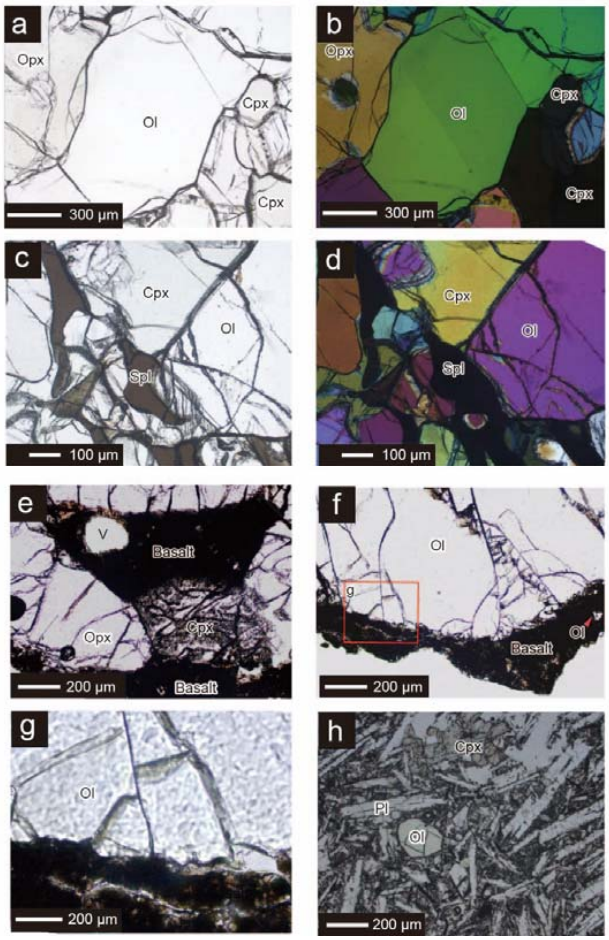

Figure 2. Photomicrographs under a polarizing microscope (one polar and crossed polar) of olivine crystals in the core of the xenolith (**a**–**d**), clinopyroxene and orthopyroxene (**e**), and olivine at the contact of the xenolith with the host basalt (**f**); extended image of the area "g" in the picture "f" (**g**); and constituent minerals of olivine basalt (**h**). Cpx, clinopyroxene; Ol, olivine; Opx, orthopyroxene; Pl, plagioclase; Spl, spinel; V, void.

The host basalt consists of olivine, clinopyroxene, and plagioclase phenocrysts (Figure 2h) and groundmass composed of euhedral plagioclase and magnetite, exhibiting intersertal texture. Olivine and clinopyroxene phenocrysts are euhedral to subhedral, and 10–200 μm in size. Plagioclase phenocrysts are euhedral to subhedral, and about 10–300 μm in size.

4.2. Chemical Compositions of Constituent Minerals

Chemical compositions of the constituent minerals of the spinel lherzolite are shown in Table 1, in which total Fe is represented as FeO, and average compositions with the standard deviations of the minerals are listed. The EMPA data indicate that olivine, orthopyroxene, clinopyroxene, and spinel are quite homogeneous in chemical composition, as shown by the standard deviations of the average values. Average Fo value and Fe content (n = 48) of olivine at the core part of the xenolith are 89.9 mol % and 0.195(3) atoms per formula unit (apfu; O = 4), respectively. Since Ejima et al. [13,17] discussed possible influence of heat from basalt magma on xenolith, the authors examined the chemical composition of olivine in contact with host basalt. EMPA analysis of olivine at the positions of 10, 15, and 30 μm from the surface resulted in $Fo_{78.3}$, $Fo_{88.7}$, and $Fo_{89.8}$ mol %, respectively, implying that, even in the olivine in contact with the basalt, the influence of the basaltic magma is limited to the very surface of olivine. The orthopyroxene is enstatite with the formula $(Mg_{0.84}Fe^{2+}_{0.09}Al_{0.05}Ca_{0.01})_{\Sigma 0.99}(Si_{0.95}Al_{0.05})_{\Sigma 1.00}O_3$ on average (n = 22). The clinopyroxene is a Na-bearing diopside: $(Na_{0.18}Ca_{0.72}Mg_{0.80}Fe^{2+}_{0.08}Cr_{0.03}Ti_{0.02}Al_{0.19})_{\Sigma 2.02}(Si_{1.88}Al_{0.12})_{\Sigma 2.00}O_6$ on average (n = 18). By assuming electronic neutrality for the stoichiometric clinopyroxene, Fe^{2+}:Fe^{3+} = 0.027:0.054 (in atoms per formula unit) is calculated, which gives the chemical formula of $(Na_{0.177}Ca_{0.715}Mg_{0.794}Fe^{2+}_{0.027}\ Fe^{3+}_{0.054}Cr_{0.028}Ti_{0.017}Al_{0.186})_{\Sigma 2.000}(Si_{1.875}Al_{0.125})_{\Sigma 2.000}O_6$. The chemical formula of spinel derived from the EMPA data is $(Mg_{0.800}Fe^{2+}_{0.212}Ni_{0.004})_{\Sigma 1.016}(Al_{1.751}Cr_{0.235})_{\Sigma 1.986}O_4$ on average (n = 36). Charge balance calculation results in 0.012 Fe^{3+} per formula unit, and, thus, the chemical formula is rewritten as $(Mg_{0.800}Fe^{2+}_{0.200}Ni_{0.004})_{\Sigma 1.004}(Al_{1.751}Cr_{0.235}Fe^{3+}_{0.012})_{\Sigma 1.998}O_4$.

Olivine phenocrysts in the host basalt have normal zoning from Fo_{79} at the core to Fo_{65} at the rim. Clinopyroxene phenocrysts are on the average composition of $(Na_{0.04}Ca_{0.86}Mg_{0.80}Fe^{2+}_{0.23}Al_{0.03}Ti_{0.05})_{\Sigma 2.01}(Si_{1.89}Al_{0.11})_{\Sigma 2.00}O_6$ (n = 23) (Table 1).

Table 1. The average chemical compositions of constituent minerals in the xenolith and basalt.

	Xenolith								Basalt			
	Olivine		Spinel		Orthopyroxene		Clinopyroxene		Olivine		Clinopyroxene	
	Av. (n = 48) *	s.d. *	Av. (n = 36) *	s.d. *	Av. (n = 22) *	s.d. *	Av. (n = 18) *	s.d. *	Av. (n = 18) *	s.d. *	Av. (n = 23) *	s.d. *
SiO_2	40.84	0.20	-	-	55.06	0.33	52.02	0.38	38.38	0.59	50.81	1.17
TiO_2	-	-	0.13	0.02	0.12	0.02	0.61	0.05	-	-	1.75	0.57
Al_2O_3	-	-	57.54	0.29	4.67	0.08	7.32	0.20	-	-	3.23	1.14
Cr_2O_3	-	-	11.52	0.20	0.40	0.03	0.97	0.07	-	-	-	-
FeO **	9.53	0.14	9.83	0.12	5.97	0.09	2.69	0.13	23.76	2.80	7.37	0.75
MnO	0.14	0.03	-	-	0.16	0.05	0.09	0.04	0.32	0.06	0.14	0.04
NiO	0.19	0.02	0.19	0.02	0.05	0.01	-	-	0.05	0.03	-	-
MgO	49.30	0.28	20.79	0.48	32.56	0.54	14.77	0.14	37.62	2.37	14.40	0.85
CaO	0.05	0.01	-	-	0.66	0.04	18.51	0.61	0.30	0.05	21.67	0.56
Na_2O	-	-	-	-	0.19	0.03	2.53	0.20	-	-	0.51	0.06
Total	100.03		100.00		99.83		99.50		100.54		99.98	
Number of Cations on the Basis of 4 Oxygens					Number of Cations on the Basis of 6 Oxygens				O = 4		O = 6	
Si	0.999	0.004	-	-	1.902	0.012	1.884	0.010	1.000	0.005	1.887	0.042
Ti	-	-	0.003	0.000	0.003	0.001	0.017	0.001	-		0.049	0.016
Al	-	-	1.751	0.006	0.190	0.003	0.312	0.009	-	-	0.142	0.050
Cr	-	-	0.235	0.005	0.011	0.001	0.028	0.002	-	-	-	-
Fe^{2+}	0.195	0.003	0.212	0.003	0.172	0.003	0.082	0.004	0.519	0.068	0.229	0.025
Mn	0.003	0.001	-	-	0.005	0.001	0.003	0.001	0.007	0.001	0.004	0.001
Ni	0.004	0.000	0.004	0.000	0.001	0.000	-	-	0.001	0.001	-	-
Mg	1.798	0.007	0.800	0.014	1.677	0.024	0.797	0.007	1.460	0.071	0.796	0.041
Ca	0.001	0.000	-	-	0.024	0.002	0.718	0.025	0.009	0.002	0.863	0.026
Na	-	-	-	-	0.013	0.002	0.178	0.014	-	-	0.037	0.004
Total	2.999		3.005		4.000		4.018		2.999		4.011	
Fo mol %	90											

* Av.: Average; s.d.: standard deviation. ** Total Fe as FeO.

4.3. Purity of the Samples Separated for Mössbauer Analysis

The minerals for Mössbauer analysis are separated from core of xenolith to avoid contact part with the host basalt. XRD patterns of each mineral dissected out from the core of the xenolith indicate no impurities, as described below. Further observation of five grains chosen from the purified grains of each mineral, using a reflection microscope and EMPA, and Raman spectroscopic analysis detected no impurities.

4.4. X-ray Powder Diffraction and X-ray Rietveld Analysis

The XRD patterns of orthopyroxene, clinopyroxene, and spinel are shown in Figure 3, indicating that the separated orthopyroxene and clinopyroxene samples are single phases, and that the spinel sample was contaminated with a very small amount of quartz, which was used for cleaning of the agate mortar.

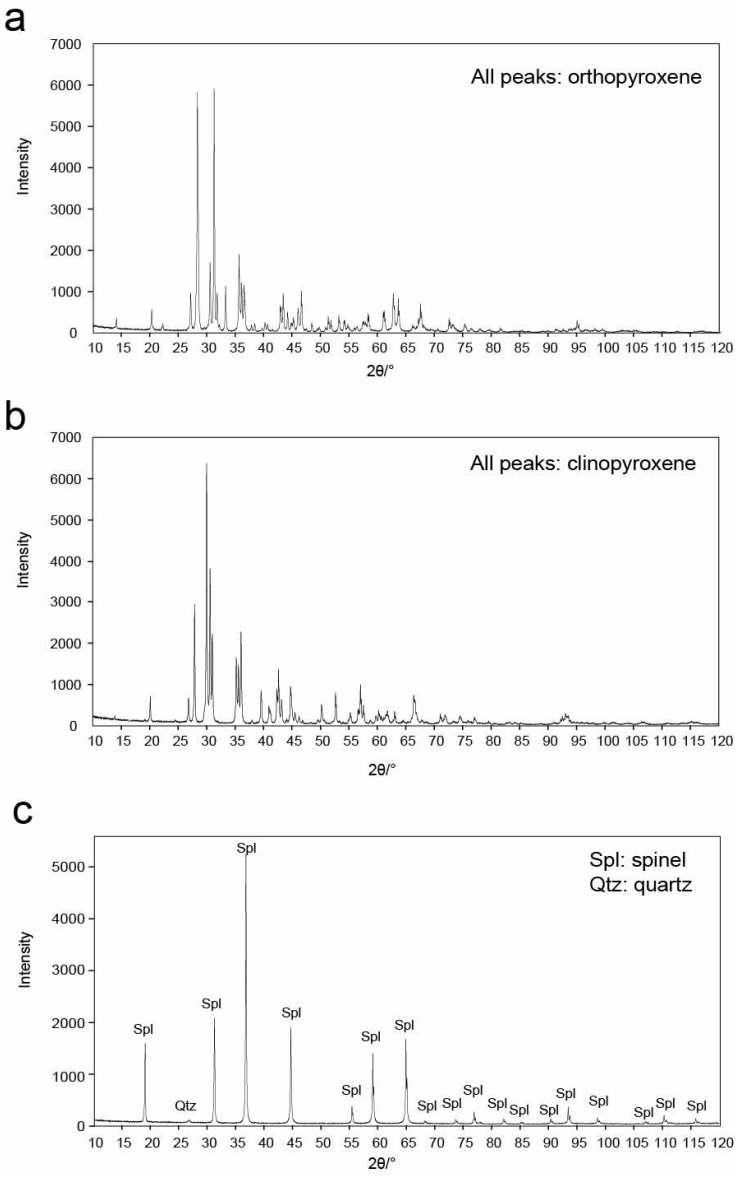

Figure 3. X-ray powder diffraction patterns of orthopyroxene (**a**), clinopyroxene (**b**), and spinel (**c**) separated from the xenolith. Mineral identification is based on the X-ray diffraction data of enstatite [25], diopside [26], and spinel [27].

Details of the X-ray diffraction data collection and the crystallographic data of olivine are shown in Table 2, and the results of the Rietveld analyses using the XRD data of the olivine are shown in Figure 4. To refine the site occupancies of Mg and Fe at the octahedral *M*1 and *M*2 sites in olivine with the structural formula $^{VI}M2^{VI}M1^{IV}TO_4$, Mg + Fe at each site was constrained to be 1.0. Site occupancy of the tetrahedral site was fixed to 1.0Si. In the structural refinement, the weighted-pattern reliability factor R_{wp} and goodness-of-fit were reduced to 12.86 and 1.26, respectively. The refined Mg and Fe occupancies are Mg = 0.902(4) and Fe = 0.098 at the *M*1 site, and Mg = 0.926(4) and Fe = 0.074 at the *M*2 site (Table 3), in which standard deviations, 1σ, are shown in the parentheses. The total Fe population per 4 oxygens is 0.172 apfu, which is close to 0.195(3) apfu given by EMPA (Table 1). The refined atomic positions are listed in Table 3.

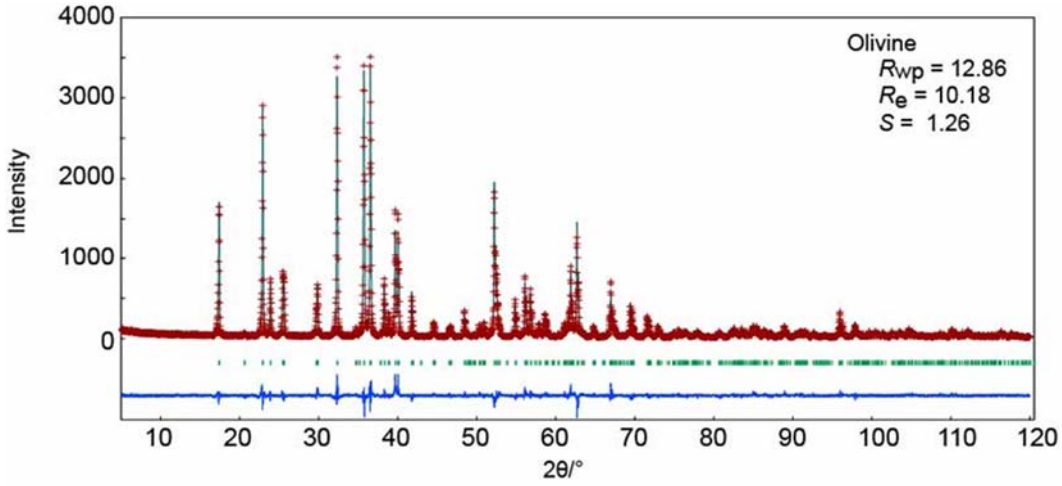

Figure 4. Observed and calculated X-ray powder diffraction patterns of the olivine separated from the xenolith. The cross marks are the observed data, the solid line is the calculated pattern, the vertical green bars mark all possible Bragg reflections ($K_{\alpha1}$ and $K_{\alpha2}$) for olivine, and the solid line at the bottom shows the difference between the observed and calculated patterns.

Table 2. Details of data collection and crystallographic data of the separated olivine grains from the core of the xenolith.

	Olivine
Radiation	Cu*K*α (λ = 1.541769 Å)
Monochromator	Graphite
2*θ* scan range (°)	5.00–120
Step interval (°2*θ*)	0.02
Max. intensity (counts)	5750
No. of phases refined	1
Space groupe	*Pbnm*
a (Å)	4.7631(1)
b (Å)	10.2284(1)
c (Å)	5.9941(1)
V (Å^3)	292.022(7)
Z	4
*D*calc (g/cm^3)	3.32
R_p (%) *	9.55
R_{wp} (%) *	12.86
R_e (%) *	10.18
S *	1.26

* R_p, *R*-pattern; R_{wp}, *R*-weighted pattern; R_e, *R*-expected; *S*, Goodness-of-fit [28].

Table 3. Site occupancies (g) *, atomic coordinates (x, y, z) *, and isotropic displacement parameters (B_{eq} in Å^2) * of the olivine.

Olivine						
Site	***n*** **	***g***	***x***	***y***	***z***	B_{eq}
*M*1	4	Mg0.902(4)Fe0.098	0	0	0	1.58(5)
*M*2	4	Mg0.926(4)Fe0.074	0.9860(4)	0.2784(1)	1/4	1.58(6)
T	4	1.0Si	0.4288(4)	0.0949(1)	1/4	1.77(5)
O1	4	1	0.7636(7)	0.0927(3)	1/4	1.8(1)
O2	4	1	0.2159(7)	0.4482(4)	1/4	1.12(9)
O3	8	1	0.2767(5)	0.1627(2)	0.0325(5)	1.81(8)

* Numbers in parentheses represent standard deviations. ** n_{eq} = multiplicity of sites.

4.5. ^{57}Fe Mössbauer Spectroscopic Analysis

The Mössbauer spectra of the separated olivine, orthopyroxene, clinopyroxene, and spinel are shown in Figure 5. The Mössbauer hyperfine parameters of the doublets, such as isomer shift (*I.S.*) and quadrupole splitting (*Q.S.*), and their assignments are presented in Table 4.

The Mössbauer spectrum of olivine consists of four doublets (Figure 5a), since Shinno et al. [29] found *I.S.* = 1.1–1.2 mm/s, *Q.S.* = 3.0–3.2 mm/s and *I.S.* = 1.1–1.2 mm/s, and *Q.S.* = 2.8–2.9 mm/s for the doublets by Fe^{2+} at the octahedral *M*2 and *M*1 sites of olivine, respectively. The doublets AA′ (*I.S.* = 1.165(2) mm/s; *Q.S.* =3.081(3) mm/s) and BB′ (*I.S.* = 1.141(2) mm/s; *Q.S.* =2.899(4) mm/s) are assigned to Fe^{2+} at the *M*2 and *M*1 sites, respectively. The doublet CC′ with *I.S.* = 0.40(2) and *Q.S.* = 0.69(3) mm/s is assigned to Fe^{3+} at *M*2 site of olivine, based on the results of Ejima and Akasaka [30] (*I.S.* = 0.38–0.40 mm/s; *Q.S.* = 0.57–0.93 mm/s). The $Fe^{3+}/\Sigma Fe$ value, determined using the area ratios of the doublets, is 0.027(2). From this result and the average Fe content obtained by EMPA, 0.195(3) apfu, Fe^{3+} in the olivine is derived as 0.005(2) apfu on average. The doublet DD′ (*I.S.* = 1.13(3) mm/s; *Q.S.* = 1.48(6) mm/s) is assigned to Fe^{2+} in spinel, as explained below. Although spinel inclusion in olivine was not detected by EMPA observation, X-ray diffraction analysis, and Raman spectroscopic analysis, the Mössbauer sample is considered to contain olivine grains including spinel inclusions.

The spectrum of orthopyroxene is fitted to three doublets (Figure 5b). Based on the hyperfine parameters of the doublets by Fe^{3+} and Fe^{2+} at the octahedral *M*1 site and of Fe^{2+} at the octahedral *M*2 site after Annersten et al. [31] (*I.S.* = 0.45 and *Q.S.* = 0.70–0.86 mm/s; *I.S.* = 1.10 and *Q.S.* = 2.77 mm/s; *I.S.* = 1.12–1.13 and *Q.S.* = 2.22–2.25 mm/s, respectively), the doublets AA′, (*I.S.* = 0.39(2) mm/s; *Q.S.* = 0.86(3) mm/s) BB′ (*I.S.* = 1.19(3) mm/s; *Q.S.* = 2.21(5) mm/s), and CC′ (*I.S.* = 1.10(5) mm/s; *Q.S.* = 2.05(10) mm/s) are assigned to Fe^{3+} at the *M*1 site, Fe^{2+} at the *M*1 site, and Fe^{2+} at the *M*2 site, respectively. The $Fe^{3+}/\Sigma Fe$ value is 0.15(1).

The spectrum of the clinopyroxene sample consists of five doublets (Figure 5c). Three doublets are assigned to Fe in clinopyroxene: the doublet AA′ (*I.S.* = 0.43(1) mm/s; *Q.S.* = 0.88(2) mm/s) corresponds to that attributed to Fe^{3+} at the octahedral *M*1 site (*I.S.* = 0.32–0.37 and *Q.S.* = 0.88–0.90 mm/s after Akasaka [32,33]; BB′ (*I.S.* = 1.06(1) mm/s; *Q.S.* = 2.00(2) mm/s) is assigned to Fe^{2+} at the 8-coordinated *M*2 site based on the data (*I.S.* = 1.10–1.14 mm/s; *Q.S.* = 1.76–1.91 mm/s) by Dowty and Lindsley (1973); and the doublet CC′ (*I.S.* = 1.09(1) mm/s; *Q.S.* = 2.54(2) mm/s) to Fe^{2+} at the *M*1 site after the data of Akasaka [33], Dowty and Lindsley [34], and Williams et al. [35] (*I.S.* = 1.14–1.19 mm/s; *Q.S.* = 2.05–2.57 mm/s). The DD′ and EE′ doublets, with *I.S.* = 0.32(1) and *Q.S.* = 0.28(2) mm/s and *I.S.* = 0.36(1) and *Q.S.* = 2.28(2) mm/s, respectively, are not consistent with ^{57}Fe Mössbauer hyperfine parameters of Fe in clinopyroxene and other minerals reported by now. As described already, clinopyroxene has the rim consisting of diopside and glass. Therefore, we assume that the doublets DD′ and EE′ are attributed to Fe in the glass of the rim of the clinopyroxene. The $Fe^{3+}/\Sigma Fe$ value of the clinopyroxene calculated from the area ratios of the doublets AA′, BB′, and CC′ is 0.26(3).

Four doublets are fitted to the Mössbauer spectrum of the separated spinel sample (Figure 5d). The doublets AA′ (*I.S.* = 0.88(2) mm/s; *Q.S.* = 1.30(3) mm/s) and BB′ (*I.S.* = 0.94(2) mm/s; *Q.S.* =

1.99(4) mm/s) are assigned to Fe^{2+} at the octahedral sites based on the data of hercynite ($FeAl_2O_4$) (*I.S.* = 0.91 mm/s; *Q.S.* = 1.57 mm/s) after Osborne et al. [36] and of ulvöspinel (Fe_2TiO_4) (*I.S.* = 0.83 mm/s; *Q.S.* = 1.91 mm/s) after Malysheva et al. [37], and CC′ (*I.S.* = 0.19 mm/s; *Q.S.* = 0.71 mm/s) is assigned to Fe^{3+} at the octahedral sites after the data (*I.S.* = 0.29 mm/s; *Q.S.* = 0.92 mm/s) by Warenborgh et al. [38]. The rather broad line width of the doublet AA′, FWHH = 0.57(9) mm/s (Table 5), suggests strong overlapping of a couple of doublets. It is considered that the doublet AA′ in our study corresponds to two doublets Fe^{2+}-(I) and Fe^{2+}-(III) of Hao and Li [14]. The doublet DD′ is not assigned to Fe in spinel, because the *I.S.* and *Q.S.* of the doublet DD′ do not fit to those of Fe^{2+} nor Fe^{3+} in spinel group minerals. It may be attributable to Fe in some inclusion that was not detected in the XRD pattern. The $Fe^{3+}/\Sigma Fe$ value of the spinel is 0.34(5).

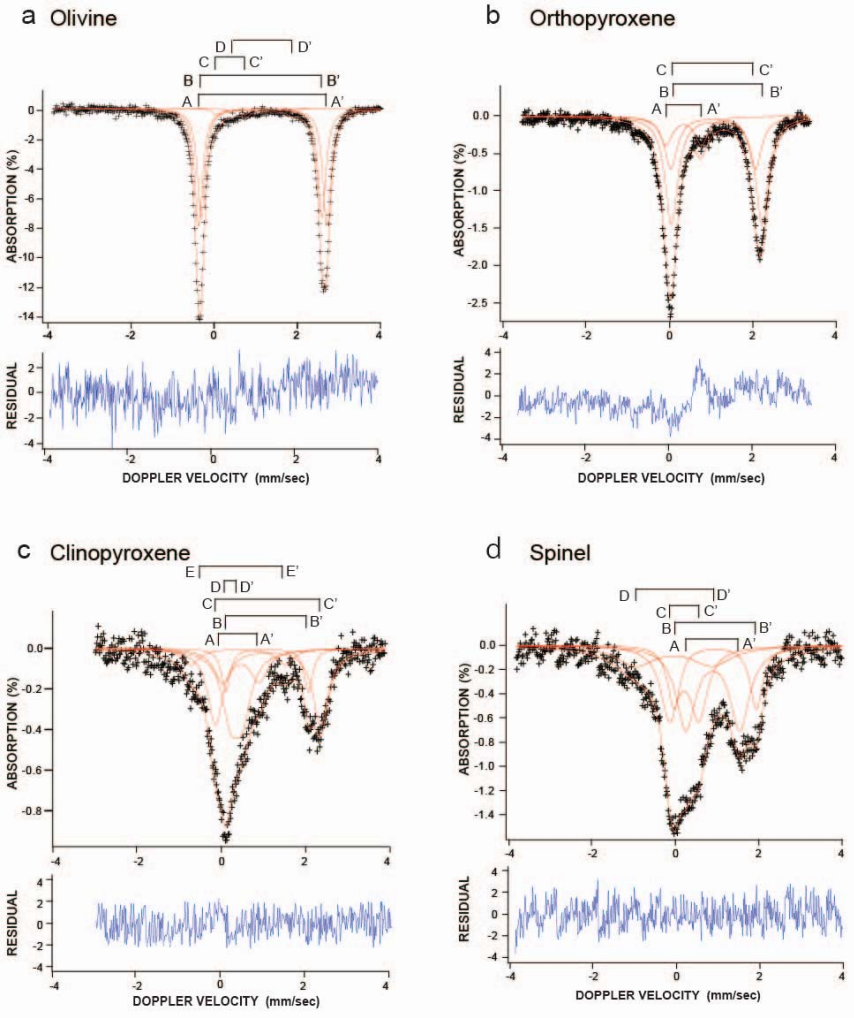

Figure 5. ^{57}Fe Mössbauer spectra of olivine (**a**), orthopyroxene (**b**), clinopyroxene (**c**), and spinel (**d**) separated from the xenolith. (**a**) The doublets AA′ and BB′ are due to Fe^{2+} of *M*2 and *M*1 in olivine, respectively. The doublet CC′ is assigned to Fe^{3+} of *M*2 site in olivine. The DD′ maybe assigned to Fe^{2+} in spinel. (**b**) AA′, BB′, and CC′ are assigned to Fe^{3+} at the octahedral *M*1 site, Fe^{2+} at the *M*1 site, and Fe^{2+} at the octahedral *M*2 site of orthopyroxene, respectively. (**c**) The doublets AA′, BB′, and CC′ are assigned to Fe^{3+} at the octahedral *M*1 site, Fe^{2+} at the 8-coordinated *M*2 site, and Fe^{2+} at the *M*1 site, respectively. The DD′ and EE′ doublets are not due to Fe in clinopyroxene and are attributable to Fe in the glass of the rim of the clinopyroxene. (**d**) The doublets AA′ and BB′ are assigned to Fe^{2+} at the octahedral sites, and CC′ is assigned to Fe^{3+} at the octahedral sites. The doublet DD′ does not fit to those of Fe^{2+} nor Fe^{3+} in spinel group minerals. It may be attributable to Fe in some inclusion that was not detected in the XRD pattern.

Table 4. ^{57}Fe Mössbauer hyperfine parameters and area ratios of the Mössbauer doublets of olivine, orthopyroxene, clinopyroxene, and spinel separates.

Mineral	Doublets	*I.S.* * (mm/s)	*Q.S* * (mm/s)	*FWHH* * (mm/s)	Area Ratio (%)	Assignments	χ^2/Freedom	Fe^{2+}:Fe^{3+}
Olivine	AA′	1.165(2)	3.081(3)	0.228(3)	49.8(14)	$^{M2}Fe^{2+}$ in olivine	1.65	97.3(14):2.7(2) **
	BB′	1.141(2)	2.899(4)	0.228(3)	46.1(14)	$^{M1}Fe^{2+}$ in olivine		
	CC′	0.40(2)	0.69(3)	0.228(3)	2.7(2)	$^{M2}Fe^{3+}$ in olivine		
	DD′	1.13(3)	1.48(6)	0.228(3)	1.4(2)	Fe^{2+} in spinel		
Orthopyroxene	AA′	0.39(2)	0.86(3)	0.38(1)	15(1)	$^{M1}Fe^{3+}$	1.14	85(8):15(1)
	BB′	1.19(3)	2.21(5)	0.38(1)	27(6)	$^{M1}Fe^{2+}$		
	CC′	1.10(5)	2.05(10)	0.38(1)	58(6)	$^{M2}Fe^{2+}$		
Clinopyroxene	AA′	0.43(1)	0.88(2)	0.51(4)	16(2)	$^{M1}Fe^{3+}$	1.21	74(4):26(3) ***
	BB′	1.06(1)	2.00(2)	0.25(4)	11(2)	$^{M2}Fe^{2+}$		
	CC′	1.09(1)	2.54(2)	0.45(3)	34(3)	$^{M1}Fe^{2+}$		
	DD′	0.32(1)	0.28(2)	0.51(4)	30(3)	Unidentified		
	EE′	0.36(1)	2.28(2)	0.51(4)	8(1)	Unidentified		
Spinel	AA′	0.88(2)	1.30(3)	0.57(9)	36(3)	Fe^{2+}	1.41	66(6):34(5) ***
	BB′	0.94(2)	1.99(4)	0.37(5)	18(7)	Fe^{2+}		
	CC′	0.19(1)	0.71(3)	0.50(4)	28(5)	Fe^{3+}		
	DD′	−0.1(2)	1.9(3)	1.2(2)	18(4)	Unidentified		

* *I.S.*, isomer shift relative to a metallic iron absorber; *Q.S.*, quadrupole splitting; *FWHH*, full width at half peak height. ** Fe^{2+} in spinel is excluded. *** The Fe^{2+}:Fe^{3+}-ratios of clinopyroxene and spinel were calculated based on the area ratios of the doublets assigned to Fe^{2+} and Fe^{3+} in each mineral.

4.6. Raman Spectroscopy, Transmission Electron Microscopy, and Electron Diffraction Analysis

Raman spectra were measured at 10 positions on the five separated olivine grains, and at 15 positions on olivine in a thin section of the core part of the xenolith. All of the Raman spectra measured match forsteriteR060551 with a composition of $(Mg_{1.82}Fe_{0.18})SiO_4$ in the Raman database (Figure 6) and no additional phases are detected.

As shown by a bright-field TEM image (Figure 7a) and a HR-TEM image of the SAED pattern of the olivine foil (Figure 7b), none of inclusion and impurity are observed in the olivine foil.

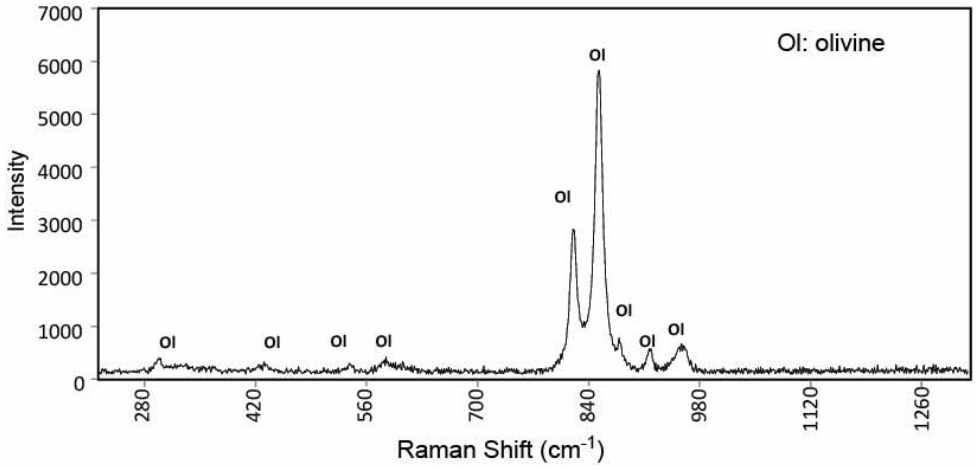

Figure 6. Raman spectrum of the separated olivine from the Tariat spinel lherzolite xenolith. Ol, olivine.

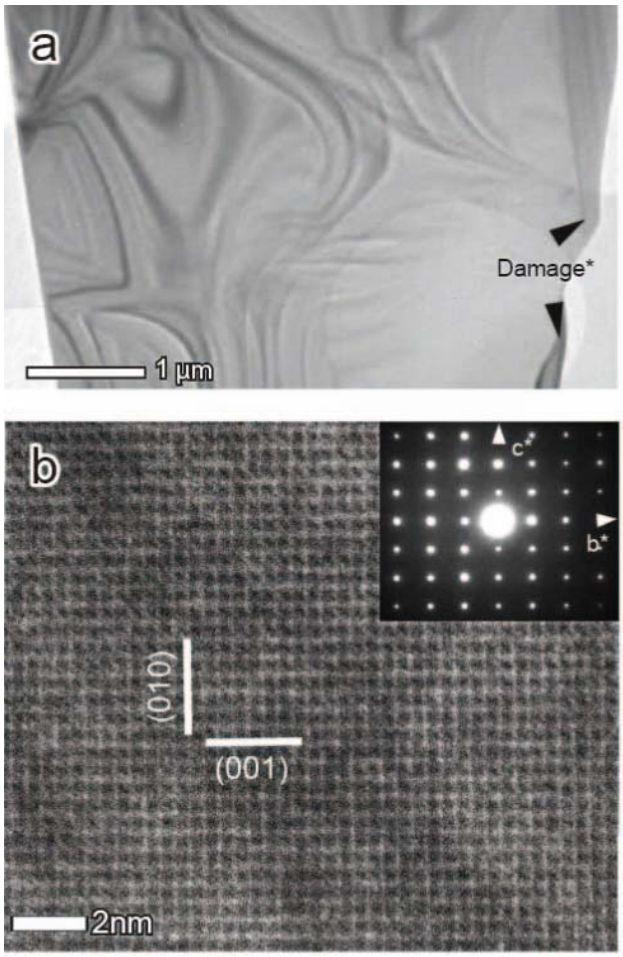

Figure 7. Bright-field TEM images of the TEM foil made from a separated olivine grain using a FIB system (**a**) and HR-TEM image and corresponding SAED pattern, looking down from the [100] direction (**b**). Damage*: Damaged area caused by the FIB milling procedure.

5. Discussion

5.1. Construction of Structural Formula of Olivine, Orthopyroxene, Clinopyroxene, and Spinel

In this study, we showed that separated olivine grains from the core of the spinel lherzolite xenolith have a small amount of ferric iron (0.027(2) in $Fe^{3+}/\Sigma Fe$ value and 0.005(2) apfu, on average). Although the Mössbauer hyperfine parameters indicate existence of Fe^{3+} cations at the *M*2 site in the olivine, laihunite and laihunite layer have not been detected by HR-TEM observation and Raman spectroscopic analysis, as described already. Thus, the structural formula of olivine determined by EMPA and Mössbauer analysis is finally constructed as $^{M2}[Mg_{0.893}Fe^{2+}_{0.098}Mn^{2+}_{0.003}Ca_{0.001}Fe^{3+}_{0.005}]^{M1}[Mg_{0.905}Fe^{2+}_{0.091}Ni_{0.004}]Si_{0.999}O_4$, in which Mn^{2+} and Ca ions are assigned to the *M*2 site based on the X-ray structural study by Ottonello et al. [39], and Ni ions to the *M*1 site after Nord et al. [40].

According to the chemical formula of enstatite, derived from the EMPA data, Fe^{3+} is not calculated by charge balance calculation, implying all Fe is ferrous iron. However, Mössbauer data shows that 15% of total Fe is Fe^{3+}, and Fe^{2+} at the *M*2 and *M*1 sites are 58(6) and 27(6)% of total Fe, respectively. The structural formula of enstatite, based on the recalculate FeO and Fe_2O_3 contents (5.07 and 1.00 wt %, respectively), is given as $^{M2}[Na_{0.013}Ca_{0.024}Mg_{0.849}Fe^{2+}_{0.100}Mn_{0.003}]_{\Sigma 0.989}$ $^{M1}[Mg_{0.825}Fe^{2+}_{0.046}Fe^{3+}_{0.026}Cr_{0.011}Ti_{0.003}Al_{0.089}]_{\Sigma 1.000}{}^{T}[Si_{1.899}Al_{0.101}]_{\Sigma 2.000}O_6$, in which the assignments

of Ca and Mn to the *M*2 site and of Al, Fe^{3+}, Cr, and Ti to the *M*1 site are based on the X-ray structural study by Nestola et al. [41].

As explained already, the Fe^{2+}:Fe^{3+}-ratio of the clinopyroxene can be estimated by charge balance calculation. However, it is well known fact that the Fe^{2+}:Fe^{3+}-ratios calculated from EMPA are generally unreliable and commonly are not consistent with those determined by Mössbauer spectroscopic analysis. The Fe^{2+}:Fe^{3+}-ratio of the clinopyroxene in this study, determined by the Mössbauer spectroscopy, is 74(4):26(3) in atomic % (Table 4), which results in the recalculated FeO and Fe_2O_3 contents of 1.99 and 0.78 wt %, respectively, and the structural formula of the clinopyroxene is calculated as $^{M2}[Na_{0.177}Ca_{0.717}Mg_{0.090}Fe^{2+}_{0.025}]_{\Sigma 1.009}{}^{M1}[Mg_{0.706}Fe^{2+}_{0.035}Fe^{3+}_{0.021}Cr_{0.028}Ti_{0.017}Al_{0.193}]_{\Sigma 1.000}{}^{T}[Si_{1.881}Al_{0.119}]_{\Sigma 2.000}O_6$.

Although charge balance calculation of spinel gave 0.012 Fe^{3+} per formula unit (O = 4), the Mössbauer spectroscopic analysis resulted in Fe^{2+}:Fe^{3+}-ratio of 66(6):34(5) in atomic %. According to the calculation of the chemical formula using recalculated FeO and Fe_2O_3 contents, 6.49 and 3.71 wt %, respectively, the chemical formula is given as $(Mg_{0.793}Fe^{2+}_{0.139}Ni_{0.004})_{\Sigma 0.936}(Al_{1.735}Cr_{0.233}Fe^{3+}_{0.071})_{\Sigma 2.039}O_4$.

5.2. Significance of Oxidation States of Fe in Olivine, Clinopyroxene, Orthopyroxene, and Spinel

5.2.1. Olivine

In the published studies of the oxidation state of Fe in olivine from mantle-derived xenoliths, only olivine in metasomatized spinel lherzolite from Dish Hill [5,6] and Oki Island [13] have been reported to contain a small amount of Fe^{3+} (0.01–0.06 $Fe^{3+}/\Sigma Fe$). However, in the former, the Fe^{3+} detected in olivine was attributed to that within laihunite layers in the olivine, which might have formed by metasomatism [42]. On the other hand, in the latter, Fe^{3+} within olivine has been proved to be located at the octahedral sites [13], but a part of Fe^{2+} within the olivine may have changed to Fe^{3+} by annealing of the xenoliths due to heat from the host magma [13,17]. In contrast, olivine from the spinel lherzolite xenolith in this study does not contain detectable inclusions, such as laihunite or precipitates, and there is no evidence of alteration by metasomatism or high-temperature oxidation. Therefore, it is concluded that the Fe^{3+} within olivine in the Tariat xenolith was generated at rather oxidized conditions in the upper mantle, where Fe^{3+} was stable.

As reviewed by Ashworth and Chambers [43], one possible mechanism by which Fe^{2+} oxidizes to Fe^{3+} in olivine is diffusion of electrons and cations [44]. The reaction of $3Fe^{2+} \Leftrightarrow 2Fe^{3+} + \square$ (vacancy) shows that one Fe^{2+} ion has to move from an octahedral site to outside of the olivine structure. In fact, Fe^{2+} ions diffuse to the edge of the olivine grain, as Mackwell [45] demonstrated in an annealing experiment of fayalite. This mechanism seems to apply reasonably to the generation of Fe^{3+} within olivine in the upper mantle if the redox conditions are suitable for oxidation of Fe^{2+} to Fe^{3+} in the olivine, as well as the case of high temperature oxidation of olivine in lavas and scoria [46–49].

Another model on the formation of Fe^{3+} in terms of diffusion of H_2O, OH, or H in olivine has been proposed by Hwang et al. [50]. If the release of H from the mantle olivine containing OH takes place during exhumation through a dehydrogenation–oxidation process [51], Fe^{3+} may be formed in the following manner: $Fe^{2+} + (OH)^- \rightarrow Fe^{3+} + O^{2-} + 0.5H_2$. This process also requires movement of one Fe atom per 3Fe atoms to the outside of olivine to maintain the charge balance. In this case, owing to the very fast diffusion rate of hydrogen, the generated Fe^{3+} would not be localized in the olivine.

The first model seems to be more suitable to our conclusion that the Fe^{3+} within olivine in the Tariat xenolith was generated at rather oxidized conditions in the upper mantle.

5.2.2. Clinopyroxene, Orthopyroxene, and Spinel

The $Fe^{3+}/\Sigma Fe$ value of the clinopyroxene in the Tariat spinel lherzolite xenolith ($Fe^{3+}/\Sigma Fe$ = 0.26) is close to the highest value in clinopyroxene ($Fe^{3+}/\Sigma Fe$ = 0.03–0.32) of spinel lherzolite xenoliths from other localities (Table 5). The $Fe^{3+}/\sum Fe$ value of the orthopyroxene ($Fe^{3+}/\Sigma Fe$ = 0.15) is also close to the highest value reported from unmetasomatized spinel lherzolite xenoliths ($Fe^{3+}/\Sigma Fe$ = 0.05–0.13).

Table 5. Published data of $Fe^{3+}/\Sigma Fe$ of minerals from spinel lherzolite xenoliths, determined by Mössbauer spectroscopic analysis.

Reference	Occarrence	Rock Type	$Fe^{3+}/\Sigma Fe$			
			Olivine	Clinopyroxene	Orthopyroxene	Spinel
Wood and Virgo [2]	Kilbourme Hole, New Mexico	Spinel-lherzolite xenolith	-	-	-	0.18–0.25
Wood and Virgo [2]	Massif Central, France	Spinel-lherzolite xenolith	-	-	-	0.25–0.28
Wood and Virgo [2]	Ichinomegata, Japan	Spinel-lherzolite xenolith	-	-	-	0.26–0.28
Wood and Virgo [2]	Tariat, Mongolia	Spinel-lherzolite xenolith	-	-	-	0.16–0.24
Wood and Virgo [2]	Vitim Plateau, Mongolia	Spinel-lherzolite xenolith	-	-	-	0.15–0.27
Canil et al. [3]	Southeastern Australia	Spinel-lherzolite xenolith	0	0.16–0.19	0.06	0.15–0.22
Canil et al. [3]	Massif Central, France	Spinel-lherzolite xenolith	0	0.19	0.05	0.26
Woodland et al. [11]	Beni Bousera, Morocco	Orogenic lherzolite massifs	0	0.03–0.14	0.02–0.06	0.02–0.13
Woodland et al. [14]	Ronda, Spain	Orogenic lherzolite massifs	0	0.06–0.19	0.04–0.08	0.08–0.26
Woodland et al. [11]	Pyrenees, France	Orogenic lherzolite massifs	0	0.19–0.32	0.05–0.07	0.10–0.27
Perinelli et al. [52]	Northern Victoria Land, Antarctica	Spinel lherzolite xenolith	-	-	-	0.17–0.23
Hao and Li [14]	Eastern China	Spinel lherzolite xenolith	0	0.22–0.31	0.05–0.13	0.14–0.23
This study	Tariat, Mongolia	Spinel lherzolite xenolith	0.03	0.26	0.15	0.34

The $Fe^{3+}/\Sigma Fe$ value of spinel in this study is 0.34, which is higher than values of spinels in Tariat spinel lherzolite ($Fe^{3+}/\Sigma Fe$ = 0.16–0.24) reported by Wood and Virgo [2] but rather similar to values of spinel from a metasomatized spinel lherzolite xenolith reported by McGuire et al. [5] and from pyroxenite by Dyar et al. [7].

Because the Tariat spinel lherzolite xenolith in this study show no evidence of metasomatism or thermal alteration, the existence of a small amount of Fe^{3+} in olivine and the fairly high Fe^{3+} contents in orthopyroxene, clinopyroxene and spinel indicate more oxidized condition at the source upper mantle of the Tariat spinel lherzolite xenolith than other districts. However, the results in the present study and of Wood and Virgo [2] indicate variable $Fe^{3+}/\Sigma Fe$ values of spinels in the Tariat spinel lherzolite. Thus, the redox condition of the source area in the upper mantle is not regarded as uniform.

5.3. Evaluation of Redox Condition of the Source Area of the Tariat Spinel Lherzolite Xenoliths

Hao and Li [14] concluded that the calculated fO_2 values on the olivine-orthopyroxene-spinel and olivine-orthopyroxene-clinopyroxene assemblages in their spinel lherzolite data set lie within the range of data provided elsewhere, mostly slightly below the fayalite-magnetite-quartz buffer. On the other hand, as concluded above, the Tariat spinel lherzolite in this study suggests rather oxidized condition of the upper mantle than other district. Thus, the Tariat spinel lherzolite in this study is expected to lie above the fayalite-magnetite-quartz buffer. Based on their calculation using geothermo-barometers on the garnet websterite and garnet lherzolite from the Tariat Depression, Osanai et al. [20] resulted in ca. 1100 °C and 17–23 kbar, which is very close pressure-temperature conditions of the previous studies (e.g., Harris et al. [53]). If we assume that the pressure-temperature condition of the Tariat spinel lherzolite xenolith in the present study is same as that of garnet-bearing mantle xenoliths from the same locality, $\Delta\log(fO_2)^{FMQ}$ (fO_2 relative to the FMQ buffer) of 3.4–3.6 in log unit is given by applying an oxygen geobarometer by Ballhaus et al. [15], $\Delta\log(fO_2)^{FMQ} = 0.27 + 2505/T - 400P/T - 6\log(X_{Fe}^{olv}) - 3200(1 - X_{Fe}^{olv})^2/T + 2\log(X_{Fe^{2+}}^{sp}) + 4\log(X_{Fe^{3+}}^{sp}) + 2630(X_{Al}^{sp})^2/T$, where P is in GPa, T in K, $X_{Fe^{3+}}^{sp}$ and $X_{Fe^{2+}}^{sp}$ the $Fe^{3+}/\Sigma Fe$ and $Al/\Sigma R^{3+}$ ratios in spinel, and X_{Fe}^{olv} and $X_{Fe^{3+}}^{sp}$ the $Fe^{2+}/(Fe^{2+} + Mg)$ ratios in olivine and spinel. According to the relationship between $\Delta\log(fO_2)^{FMQ}$ and $Cr/(Cr + Al)$ in spinel, shown by Ballhause et al. [15], $\Delta\log(fO_2)^{FMQ}$ values of the primitive peridotite xenoliths and metasomatized ones are ca. −3 to −1 and ca. −1 to 1 in log unit. Thus, the $\Delta\log(fO_2)^{FMQ}$ value of the Tariat spinel lherzolite xenolith in the present study indicates higher fO_2 conditions (above FMQ buffer) than those of the primitive or metasomatized peridotite xenoliths reported so far, and is consistent with the oxidation state of Fe and high Fe^{3+} contents in the constituent minerals.

However, as discussed above, the source area of the Tariat spinel lherzolite xenoliths in the upper mantle is regarded as not uniform in redox condition. Therefore, further study for the additional Tariat xenoliths is required to clarify the variation of redox conditions in the upper mantle of the Tariat Depression area.

Author Contributions: T.E. and Y.O. conceived and designed the project; Y.O., N.N., T.A. and J.S. performed the field investigation and sample collection; T.E. prepared the study samples; T.E. performed and validated the analyses by EMPA, Raman spectroscopy, TEM, X-ray Rietveld method, and Mössbauer spectroscopy; Y.K., H.O. and M.A. participated and discussed the EMPA, TEM and Mössbauer analyses, respectively; T.E. wrote the paper.

Acknowledgments: We thank Fujio Izumi and Koichi Momma of the National Institute for Materials Science for their permission to use the RIETAN-FP and VESTA programs. We appreciate valuable and constructive comments by three anonymous reviewers. This work was supported by a Grant-in-Aid for Research Activity Start-up from the Japan Society for the Promotion of Science (JSPS).

Conflicts of Interest: The authors declare no conflict of interest.

References

1. Dyar, M.D.; McGuire, A.V. Redox equilibria and crystal chemistry of coexisting minerals from spinel lherzolite mantle xenoliths. *Am. Mineral.* **1989**, *74*, 969–980.

2. Wood, B.J.; Virgo, D. Upper mantle oxidation state: Ferric iron contents of lherzolite spinels by ^{57}Fe Mössbauer spectroscopy and resultant oxygen fugacities. *Geochimica et Cosmochimica Acta* **1989**, *53*, 1277–1291. [CrossRef]
3. Canil, D.; Virgo, D.; Scarfe, C.M. Oxidation states of mantle xenoliths from British Columbia, Canada. *Contrib. Mineral. Petrol.* **1990**, *104*, 453–562. [CrossRef]
4. Bryndzia, L.T.; Wood, B.J. Oxygen thermobarometry of abyssal spinel peridotites: The redox state and C-O-H volatile composition of the Earth's suboceanic upper mantle. *Am. J. Sci.* **1990**, *290*, 1093–1116. [CrossRef]
5. McGuire, A.V.; Dayr, M.D.; Nielson, J.E. Metasomatic oxidation of upper mantle peridotite. *Contrib. Mineral. Petrol.* **1991**, *109*, 252–264. [CrossRef]
6. Banfield, J.F.; Dyar, M.; Mcguire, A.V. The defect microstructure of oxidized mantle olivine from Dish Hill, California. *Am. Mineral.* **1992**, *77*, 977–986.
7. Dyar, M.D.; McGuire, A.V.; Harrell, M.D. Crystal chemistry of iron in the two styles of metasomatism in the upper mantle. *Geochimica et Cosmochimica Acta* **1992**, *56*, 2579–2586. [CrossRef]
8. Canil, D.; O'Neill, H.S.C.; Pearson, D.G.; Rudnick, R.L.; McDonough, W.F.; Carswell, D.A. Ferric iron in peridotites and mantle oxidation states. *Earth Planet. Sci. Lett.* **1994**, *123*, 205–220. [CrossRef]
9. Woodland, A.B.; Koch, M. Variation in oxygen fugacity with depth in the upper mantle beneath the Kaapvaal Craton, southern Africa. *Earth Planet. Sci. Lett.* **2003**, *214*, 295–310. [CrossRef]
10. McCammon, C.A.; Frost, D.J.; Smyth, J.R.; Laustsen, H.M.S.; Kawamoto, T.; Ross, N.L.; van Aken, P.A. Oxidation state of iron in hydrous mantle phases: Implications for subduction and mantle oxygen fugacity. *Phys. Earth Planet. Inter.* **2004**, *143*, 157–169. [CrossRef]
11. Woodland, A.B.; Kornprobst, J.; Tabit, A. Ferric iron in orogenic lherzolite massifs and controls of oxygen fugacity in the upper mantle. *Lithos* **2006**, *89*, 222–241. [CrossRef]
12. McCammon, C.A. Microscopic to macroscopic behavior: The influence of iron electronic state. *J. Mineral. Petrol. Sci.* **2006**, *101*, 130–140. [CrossRef]
13. Ejima, T.; Akasaka, M.; Ohfuji, H. Oxidation state of Fe in olivine in a lherzolite xenolith from Oku district, Oki-Dogo Island, Shimane Prefecture, Japan. *J. Mineral. Petrol. Sci.* **2011**, *106*, 246–254. [CrossRef]
14. Hao, X.L.; Li, Y.L. ^{57}Fe Mossbauer spectroscopy of mineral assemblage in mantle spinel lherzolites from Cenozoic alkali basalt, eastern China: Petrological applications. *Lithos* **2013**, *156–159*, 112–119. [CrossRef]
15. Ballhaus, C.; Berry, R.F.; Green, D.H. High pressure experimental calibration of the olivine-orthopyroxene-spinel oxygen geobarometer: Implications for the oxidation state of the upper mantle. *Contrib. Mineral. Petrol.* **1991**, *107*, 27–40. [CrossRef]
16. Forst, D.J.; McCammon, C.A. The Redox state of Earth's Mantle. *Annu. Rev. Earth Planet. Sci.* **2008**, *36*, 389–420. [CrossRef]
17. Ejima, T.; Akasaka, M.; Ohfuji, H. Ferric iron within olivine in a lherzolite xenolith from Oku district, Oki-Dogo Island, Shimane Prefecture, Japan. In Proceedings of the 21st General Meeting of the International Mineralogical Association, Johannesburg, South Africa, 1–5 September 2014.
18. Stosch, H.G.; Lugmair, G.W.; Kovalenko, V.I. Spinel peridotite xenoliths from the Tariat Depression, Mongolia. II: Geochemistry and Nd and Sr isotopic composition and their implications for the evolution of the subcontinental lithosphere. *Geochimica et Cosmochimica Acta* **1986**, *50*, 2601–2614. [CrossRef]
19. Preß, S.; Witt, H.; Seck, D.; Eonov, D.; Kovalenko, V.I. Spinel peridotite xenoliths from the Tariat Depression, Mongolia. I: Major element chemistry and mineralogy of a primitive mantle xenolith suite. *Geochimica et Cosmochimica Acta* **1986**, *50*, 2587–2599. [CrossRef]
20. Osanai, Y.; Nakano, N.; Adachi, T.; Owada, M.; Satis-Kumar, M.; Jargalan, S.; Boldbaatar, C.; Yonemura, K.; Yoshimoto, A. Garnet, Clinopyroxene megacrysts and Garnet-bearing mantle xenoliths from the Tariat Depression, Mongolia. In Proceedings of the Abstracts with Programs for the 2011 Annual Meeting of the Mineralogical Society of Japan, the Mineralogical Society of Japan, Ibaraki, Japan, 9 September 2011; p. 102. [CrossRef]
21. Irifune, T.; Isshiki, M.; Sakamoto, S. Transmission electron microscope observation of the high-pressure form of magnesite retrieved from laser heated diamond anvil cell. *Earth Planet. Sci. Lett.* **2005**, *239*, 98–105. [CrossRef]
22. Izumi, F.; Momma, K. Three-dimensional visualization in powder diffraction. *Solid State Phenom.* **2007**, *130*, 15–20. [CrossRef]

23. Dollase, W.A. Correction of intensities for preferred orientation in powder diffractometry: Application of the March model. *J. Appl. Crystallogr.* **1986**, *19*, 267–272. [CrossRef]
24. Akasaka, M.; Shinno, I. Mössbauer spectroscopy and its recent application to silicate mineralogy. *J. Mineral. Soc. Jpn.* **1992**, *21*, 3–20, (In Japanese with English Abstract). [CrossRef]
25. Yang, H.; Ghose, S. A transitional structural state and anomalous Fe-Mg order-disorder in Mg-rich orthopyroxene, $(Mg_{0.75}Fe_{0.25})_2Si_2O_6$. *Am. Mineral.* **1995**, *80*, 9–20. [CrossRef]
26. Cameron, M.; Sueno, S.; Prewitt, C.T.; Papike, J.J. High-temperature crystal chemistry of acmite, diopside, jadeite, spodumene, and ureyite. *Am. Mineral.* **1973**, *58*, 594–618.
27. Peterson, R.C.; Lager, G.A.; Hitterman, R.L. A time-of-flight neutron powder diffraction study of $MgAl_2O_4$ at temperatures up to 1273 K. *Am. Mineral.* **1991**, *76*, 1455–1458.
28. Young, R.A. Introduction to the Rietveld method. In *The Rietveld Method*; Young, R.A., Ed.; Oxford Science Publications: Oxford, UK, 1993; pp. 1–38. ISBN 9780198559122.
29. Shinno, I.; Hayashi, M.; Kuroda, Y. Mössbauer studies of olivines. *Mineral. J.* **1974**, *7*, 344–358. [CrossRef]
30. Ejima, T.; Akasaka, M. Fe^{2+}/Fe^{3+} ratios in olivine estimated using an Electron Microprobe Analyzer verified by ^{57}Fe Mössbauer spectroscopy. *Jpn. Mag. Mineral. Petrol. Sci.* **2011**, *40*, 55–62. [CrossRef]
31. Annersten, H.; Olesch, M.; Seifert, F.A. Ferric iron in orthopyroxene: A Mössbauer spectroscopic study. *Lithos* **1987**, *11*, 301–310. [CrossRef]
32. Akasaka, M. ^{57}Fe Mössbauer study of clinopyroxenes in the join $CaFe^{3+}AlSiO_6$-$CaTiAl_2O_6$. *Phys. Chem. Miner.* **1983**, *9*, 205–211. [CrossRef]
33. Akasaka, M. Clinopyroxene on the join $CaMgSi_2O_6$-$CaFe^{3+}AlSiO_6$-$CaTiAl_2O_6$ at low oxygen fugacity. *Proc. Indian Acad. Sci. (Earth Planet. Sci.)* **1990**, *99*, 39–48. [CrossRef]
34. Dowty, E.; Lindsley, D.H. Mössbauer spectra of synthetic hedenbergite-ferrosilite pyroxenes. *Am. Mineral.* **1973**, *58*, 850–868.
35. Williams, P.G.L.; Bancroft, G.M.; Bown, M.G.; Turnock, A.C. Anomalous Mössbauer Spectra of C2/c clinopyroxenes. *Nat. Phys. Sci.* **1971**, *230*, 149–151. [CrossRef]
36. Osborne, M.D.; Fleet, M.E.; Bancroft, G.M. Fe^{2+}-Fe^{3+} ordering in chromite and Cr-bearing spinels. *Contrib. Mineral. Petrol.* **1981**, *77*, 251–255. [CrossRef]
37. Malysheva, T.V.; Polyakova, N.P.; Mishin, N.E. Mössbauer spectroscopy study of lunar soil sampled by Luna 24 space probe. *Geokhimiya* **1978**, *6*, 835–841.
38. Warenborgh, J.C.; Annersten, H.; Ericsson, T.; Figueiredo, M.O.; Cabral, J.M.P.A. A Mössbauer study of natural gahnite spinels showing strongly temperature-dependent quadrupole splitting distributions. *Eur. J. Mineral.* **1990**, *2*, 267–271. [CrossRef]
39. Ottonello, G.; Principalle, F.; Della Giusta, A. Temperature, composition, and fO_2 effects on intersite distribution of Mg and Fe^{2+} in olivines. *Phys. Chem. Miner.* **1990**, *17*, 301–312. [CrossRef]
40. Nord, A.G.; Annersten, H.; Filippidis, A. The cation distribution in synthetic Mg-Fe-Ni olivines. *Am. Mineral.* **1982**, *67*, 1206–1211.
41. Nestola, F.; Ballaran, T.B.; Balic-Zunic, T.; Secco, L.; Dal Negro, A. High-pressure behavior of an Al- and Fe-rich natural orthopyroxene. *Am. Mineral.* **2008**, *93*, 644–652. [CrossRef]
42. Banfield, J.F.; Veblen, D.R.; Jones, B.F. Transmission electron microscopy of subsolidus oxidation and weathering of olivine. *Contrib. Mineral. Petrol.* **1990**, *106*, 110–123. [CrossRef]
43. Ashworth, J.R.; Chambers, A.D. Symplectic reaction in olivine and the controls of intergrowth spacing in symplectites. *J. Petrol.* **2000**, *41*, 285–304. [CrossRef]
44. Morioka, M.; Nagasawa, H. Ionic diffusion in olivine. In *Diffusion, Atomic Ordering and Mass Transport: Selected Topics in Geochemistry*; Ganguly, J., Ed.; Springer: Berlin, Germany; New York, NY, USA, 1991; Volume 8, pp. 176–197. ISBN 978-1-4613-9021-3.
45. Mackwell, S.J. Oxidation kinetics of fayalite (Fe_2SiO_4). *Phys. Chem. Miner.* **1992**, *19*, 220–228. [CrossRef]
46. Ejima, T.; Akasaka, M.; Nagao, T.; Ohfuji, H. Oxidation state of Fe in olivine in andesitic scoria from Kasayama volcano, Hagi, Yamaguchi Prefecture, Japan. *J. Mineral. Petrol. Sci.* **2012**, *107*, 215–225. [CrossRef]
47. Ejima, T.; Akasaka, M.; Nagao, T.; Ohfuji, H. Oxidation states of Fe and precipitates within olivine from orthopyroxene-olivine-clinopyroxene andesite lava from Kasayama volcano, Hagi, Yamaguchi, Japan. *J. Mineral. Petrol. Sci.* **2013**, *108*, 25–36. [CrossRef]

48. Ejima, T.; Akasaka, M.; Nagao, T.; Ohfuji, H. Occurrence of Fe^{3+} and formation process of precipitates within oxidized olivine phenocrysts in basalt lava from Kuroshima volcano, Goto Islands, Nagasaki, Japan. *Mineral. Mag.* **2015**, *79*, 1833–1848. [CrossRef]
49. Ejima, T. Oxidation state of Fe within olivine phenocryst in Kami-Kometsuka scoria, Kami-Kometsuka, Aso, Kumamoto Prefecture, Japan: Effect of high temperature oxidation on the scoria. *Jpn. Mag. Mineral. Petrol. Sci.* **2015**, *44*, 323–328, (In Japanese with English Abstract). [CrossRef]
50. Hwang, S.L.; Yui, T.F.; Chu, H.T.; Shen, P.; Lizuka, Y.; Yang, H.Y.; Yang, J.; Xu, Z. Hematite and magnetite precipitates in olivine from the Sulu peridotite: A result of dehydrogenation-oxidation reaction of mantle olivine? *Am. Mineral.* **2008**, *93*, 1051–1060. [CrossRef]
51. Ingrin, J.; Skogby, H. Hydrogen in nominally anhydrous upper-mantle minerals: Concentration levels and implications. *Eur. J. Mineral.* **2000**, *12*, 543–570. [CrossRef]
52. Perinelli, C.; Andreozzi, G.B.; Conte, A.M.; Oberti, R.; Armienti, P. Redox state of subcontinental lithospheric mantle and relationships with metasomatism: Insights from spinel peridotites from northern Victoria Land (Antarctica). *Contrib. Mineral. Petrol.* **2012**, *164*, 1053–1067. [CrossRef]
53. Harris, N.; Hunt, A.; Parkinson, I.; Tindle, A.; Yondon, M.; Hammond, S. Tectonic implications of garnet-bearing mantle xenoliths exhumed by Quaternary magmatism in the Hangay dome, central Mongolia. *Contrib. Mineral. Petrol.* **2010**, *160*, 67–81. [CrossRef]

© 2018 by the authors. Licensee MDPI, Basel, Switzerland. This article is an open access article distributed under the terms and conditions of the Creative Commons Attribution (CC BY) license (http://creativecommons.org/licenses/by/4.0/).